Influence of Grain-Scale Properties on Localization Patterns and Slip Weakening within Dense Granular Fault gouges

N. Casas [1,2], G. Mollon[1], and A. Daouadji[2]

[1] Univ. Lyon, INSA-Lyon, CNRS UMR5259, LaMCoS, F-69621, France.

[2] Univ. Lyon, INSA-Lyon, GEOMAS, F-69621, France.

Nathalie Casas (nath27casas@gmail.com)

Key Points:

- 2D-DEM simulations performed on numerical fault gouges composed of a very dense assembly of polygonal-shaped particles
- A small change in grain-scale gouge properties impacts Riedel shear bands formation, their orientation angle and the type of Riedel structure formed
- High interparticle friction and high bulk shear modulus increase the breakdown energy and the occurrence of dynamic slip instabilities

Plain Language Summary

The center of a seismic fault zone is usually composed of a material with granular particles highly contributing to the way the fault moves. This zone may be composed of various infill materials from mineral cementation to smaller particles that can fill remaining pore spaces between larger particles and change the properties of the fault zone. We aim to understand and reproduce the influence of grain-scale characteristics on slip mechanisms by employing numerical simulations. A variation of granular particle characteristics leads to different deformation patterns that can be identified as an indicator of a change in slip stability. The obtained results suggest that some granular materials with high interparticle friction or a high bulk shear modulus, increase the possible occurrence of dynamic slip instabilities which may lead to faster earthquake ruptures. This work investigates in more depth the link between the characteristics of the granular material, the deformations of the fault core, and the possible occurrence of an earthquake.

Abstract

Fault zones are usually composed of a granular gouge, coming from the wear material of previous slips, which contributes to friction stability. Once considering a mature enough fault zone that has already been sheared, different types of infill materials can be observed, from mineral cementation to matrix particles that can fill remaining pore spaces between clasts and change the rheological and frictional behaviors of the gouge. We aim to understand and reproduce the influence of grain-scale characteristics on slip mechanisms and gouge rheology (Riedel bands) by employing the Discrete Element Method. A 2D-direct shear model is considered with a dense assembly of small polygonal cells of matrix particles. A variation of gouge characteristics such as interparticle friction, gouge shear modulus or the number of particles within the gouge thickness leads to different Riedel shear bands formation and orientation that has been identified as an indicator of a change in slip stability (Byerlee et al., 1978). Interpreting results with slip weakening theory, our simulated gouge materials with high interparticle friction or a high bulk shear modulus, increase the possible occurrence of dynamic slip instabilities (small nucleation length and high breakdown energy). They may give rise to faster earthquake ruptures.

1. Introduction

Within the fault core, the fault gouge is known to deeply contribute to friction stability [(Marone & Scholz, 1988), (Reches & Lockner, 2010)] and to play an important role in the sudden energy release during seismic sliding (Sammis et al., 1987). For local fault scale studies, one of the key points remains to be able to relate geological and physical properties of the gouge to the slip behavior and types of dynamic slip instabilities [(Leeman et al., 2015), (Collettini et al., 2019)]. One way to determine the laboratory rock failure stability is to compare the loading stiffness of the fault with its weakening rate. The friction within gouge sliding can then be modeled either with classical Slip dependent laws or Rate-and-State friction laws to compare the weakening rate K_c to the fault stiffness K and infer on dynamic slip occurrence and behaviors [(Dieterich, 1972), (Scholz et al., 1972), (Ohnaka, 2013), (Spagnuolo et al., 2016), (Im et al., 2019), (Scuderi et al., 2020)]. Slip instabilities may occur if the loading stiffness of the fault K (i.e. stiffness of the loading system) appears to be lower than K_c ($K_c > K$).

This weakening rate is also related to the breakdown energy released during the slip. The total energy budget ΔW ($J.m^{-2}$) associated with this rupture propagation, also based on classical slip weakening models [(Kanamori & Heaton, 2000), (Rice & Cocco, 2002), (Abercrombie & Rice, 2005), (Aubry et al., 2018)], is the total deformation energy dissipated in the fault process and the sum of a breakdown energy E_B (on-fault energy), a radiated energy E_R (off-fault energy propagating by the mean of elastic waves) and a frictional energy E_H (dissipated within the slip zone by frictional heating). The post-peak rupture energy E_B, or Breakdown Energy, is the energy needed to weaken the fault. While E_B was often assimilated to the fracture energy G_c (Abercrombie & Rice, 2005), it is now useful to differentiate that the breakdown work appears to be the sum of the fracture energy (the very first peak of weakening) and the overshoot energy or other second weakening process [(Paglialunga et al., 2021), (Ke et al., 2022), (Casas et al., 2022)].

Previous analysis of fault zone rheology has shown that the onset of instabilities requires some shear localization (i.e. fault fabric development), although the reverse proposition is not necessarily true. These shear deformations are complex structures, that can be observed at specific Riedel angles (Tchalenko, 1970). They have been the subject of considerable interest for many years [(Riedel, 1929), (Byerlee, 1978), (Katz & Weinberger, 2005), (Haines et al., 2013), (Hadizadeh et al., 2015), (Scuderi et al., 2020)], and reflect a heterogeneous stress field developing in response to deformation [(Marone & Scholz, 1989), (Morgan & Boettcher, 1999), (Kaminskaite et al., 2019)]. The presence of these Riedel bands has been identified as potentially responsible for mechanical weakening [(Gu & Wong, 1994), (Beeler et al., 1996)] and they can be both associated with slow-slip events or fast earthquakes. The angle between Riedel bands and the direction of shearing, depending on the physical properties of the fault gouge, is also an indicator of a change in slip stability (Byerlee et al., 1978). However, the link between the angle orientation of Riedel bands and slip patterns is not yet fully understood.

In this paper, the slip mechanism studied takes place in a mature fault, i.e. a fault that has already lived numerous successive slips during previous geological times. This fault may have been cemented over time without slip, due to rock dissolution or partial melting [(Walderhaug, 1994), (Di Toro et al., 2009), (Fondriest et al., 2020), (Rodrigues et al., 2021)], or filled with matrix particles (i.e. very thin cohesionless particles) produced by local comminution (Daouadji & Hicher, 2010) or by the introduction of other sediments within the fault gouge [(Lee & Kim, 2005), (Woodcock & Mort, 2008)]. In (Casas et al., 2022), we simulated a cemented granular fault gouge (dry contact) with 2-D Discrete Element Modeling (DEM), establishing a link between the initial amount of porosity and cementation within the gouge and the type of rheological behavior observed. In order to have a better understanding of the link between grain-scale properties and gouge-scale deformations through Riedel shear bands evolution, another 2D-DEM model is proposed hereafter, focusing on thin matrix particles. This granular medium represents a highly dense packing of particles revealing Riedel bands formation with direct shear experiments. The first section presents the numerical model and granular materials used for the study. Then the second part of this paper is devoted to the study of the timing of Riedel bands formation and evolution as a function of gouge characteristics. All the lithologic variations presented are then summarized into only three main parameters: the interparticle friction (micro-scale), the effective shear modulus of the gouge layer (macro-scale), and the ratio of gouge thickness to grain size (i.e. number of particles within the gouge thickness). In the last section, the roles of these three parameters are discussed by comparing Riedel angle orientation and effective friction peak. Then, the obtained results are interpreted according to a very simplified model such as the linear slip weakening model, to establish a connection with the occurrence of dynamic slip instabilities.

2. Methodology for sheared fault gouge modeling

Even though certain continuous methods are used to model geological fault structures (Lynch & Richards, 2001), they commonly face difficulties in reproducing experimental observations due to the continuity assumption they need to adopt. As an alternative to the classical Finite Element Method (FEM) and Finite Difference Method (FDM), the Discrete Element Method (DEM) describes the flow of granular materials where each particle has its own behaviors and

interactions with its neighbors [(Cundall & Strack, 1979), (Potyondy & Cundall, 2004)]. The DEM has been successfully used in fault mechanics to understand some frictional and contact properties inside the fault core [(Morgan & Boettcher, 1999), (Morgan, 1999), (Guo & Morgan, 2004), (Aharonov & Sparks, 2004), (Da Cruz et al., 2005), (Cho et al., 2008), (Zhao et al., 2012), (Zhao, 2013), (Ferdowsi et al., 2014), (Dorostkar et al., 2017a), (Dorostkar et al., 2017b), (Gao et al., 2018), (Ferdowsi & Rubin, 2020), (Mollon et al., 2021)]. It enables to observe the nucleation and propagation of discrete structures during shearing. In this study, the code MELODY2D is used for the simulation of a 2D fault gouge [(Mollon, 2016), (Mollon, 2018)]. This is a C++ code allowing to simulate of a broad variety of granular media in two dimensions. In this numerical framework, each particle has its own motion and trajectory, driven by Newton's laws of motion. The motion is controlled by user-defined and physics-based contact interactions, Figure 1 (a). In the present case, each contact is based on standard frictional contact laws. The contour of each grain is discretized by a piecewise linear frontier with nodes and segments, and a two-pass node-to-segment contact algorithm is employed [(Mollon, 2018), (Casas et al., 2022)], to avoid interpenetrations between very irregular non-convex particles.

We also underline the importance of using non-circular particles for rigid bodies, since this choice has a strong influence on the effective friction measured within the gouge [(Mair et al., 2002), (Nouguier-lehon et al., 2003), (Anthony & Marone, 2005), (Mollon et al., 2020)]. A granular sample with only matrix particles is created as a dense assembly of small polygonal cells. This work is seen as the first step toward future simulations considering mixtures of angular grains surrounded by matrix cells representing a matrix of fines. To generate this kind of granular medium, a small code called Cvoro (C++) using a Voronoï tessellation algorithm (Mollon & Zhao, 2012) allows the creation of a dense packing of polygonal particles. For this model, an almost constant size of cells is considered for all particles ($\emptyset_{eq} \approx 20\ \mu m$), with slightly irregular polygons, Figure 1 (b). For an initial gouge thickness equal to $2\ mm$, consistent with the literature [(Biegel et al., 1989), (Rice & Cocco, 2002)], the length of the gouge is settled to $20\ mm$ in order to have a Representative Surface Element and be able to observe sufficient shear deformations, as performed in (Casas et al., 2021). To be able to realize parametric studies, a "Matrix-Sample" (M-S) is defined as a reference model (summary of characteristics in *Table S1*). An interesting point is that the initial porosity within the gouge is negligible here ($\ll 1\ \%$), resulting in an extremely dense compacted sample.

The granular matrix is then submitted to direct shear experiments, Figure 1 (c). The lower rock wall is fixed in displacement and a normal stress of $40\ MPa$ and slip velocity of $1\ m/s$ are imposed on the upper rock wall. Periodic boundary conditions are present on both right- and left-hand sides of the sample to maintain the continuity of the movement at large slips, but the upper rock wall can freely move in the y-direction to allow dilatancy to take place. These boundary conditions with non-deformable walls can induce differences in the results found with those of the literature studying stick-slip experiments (in particular, in the formation of the Riedel bands). A dry contact model is considered with rigid bodies (rock density equal to 2600 kg/m^3) and without gravity. A Coulomb friction contact law is also adopted, meaning that every contact between particles depends on the interparticle friction μ_{num}, contact stiffnesses k_n and a numerical damping γ. In the (M-S) reference sample μ_{num} is equal to 0.3 to test the

property of matrix particles as a weak material with limited friction, k_n is constant and equal to 10^{15} Pa/m for (M-S) and derived from numerical calibration realized by (Casas et al., 2022), and, γ is set to 0.2. To avoid wall-slip effects which occur with smooth boundaries, an arbitrarily high cohesion of 500 MPa is introduced at the interface between matrix and rock walls. It enables the creation of a certain roughness by cementing particles of the top and bottom layers to their respective boundaries. We also checked that the inertial number remains lower than 10^{-3} in order to avoid any inertial effect with the gouge shearing and to remain in a quasi-static dense granular flow (Da Cruz et al., 2005). Finally, independent numerical biaxial simulations were run (*Text S2 and Figure S1*) to recover Coulomb-Mohr data and compare samples to values of real rocks, (*Table S2 and Figure S2*). For the reference case, almost no cohesion is observed for matrix material (6.4 MPa) in the sense of Coulomb-Mohr, with an internal friction angle φ equal to 43.3°. The resulting Elasticity modulus equals 19 GPa and increases with increasing contact stiffness.

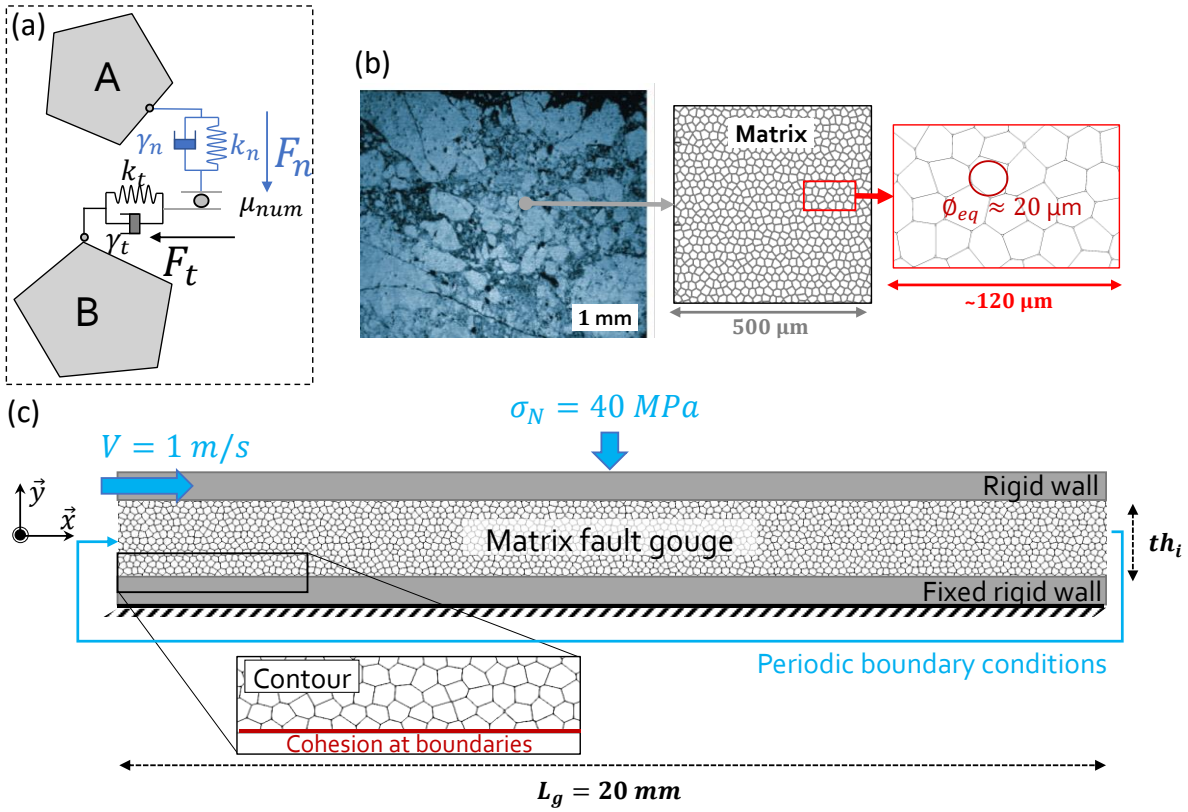

Figure 1. (a) Sketch of a DEM contact between two particles A & B, constituted by interparticle friction μ_{num} and stiffness k_n and k_t, and damping γ_n and γ_t which are numerical parameters; (b) Matrix material shape and size: left, image from (Riedmüller et al., 2001); center, zoom in on a 500 μm x 500 μm square part ; right, zoom in on this sample with grains of equivalent diameter $\Phi_{eq} = 20$ µm; (c) DEM model of a direct shear experiment with granular fault gouge composed of 115 825 matrix particles (for the reference sample). V is the applied shearing velocity of 1 m/s, σ_N is the normal stress of 40 MPa, th_i is the initial gouge thickness of 2 mm (only for the reference sample). The first simulation step consists in compacting the sample with a normal stress of 40 MPa to create a stabilized packing of granular material. As the generated sample is already very compact, this compaction stage is only influenced by the numerical stiffness and interparticle friction inserted between particles in contact. At the end of the compaction the sample is almost identical, but with a little interpenetration between particles (~ 0.1 % of the size of the particle) which provides mechanical equilibrium.

3. Results

3.1. Typical results for the reference sample

This subsection aims to present typical results obtained for the reference granular sample (M-S), as it will be used for comparison in the rest of the paper. Typical effective friction $\mu^* = \tau/\sigma_N$ and dilation $\varepsilon_y = \Delta th/th_i$ (the thickness variation Δth in the vertical direction, divided by the initial granular sample thickness) are presented in Figure 2. Effective friction is recovered at the interface between the gouge and the upper rock wall, with τ depending on the normal stress applied to the rock wall. Shear deformation profiles are observed at different times of the simulation thanks to the solid fraction which enables underlining zones of slip and shear concentration, Figure 3.

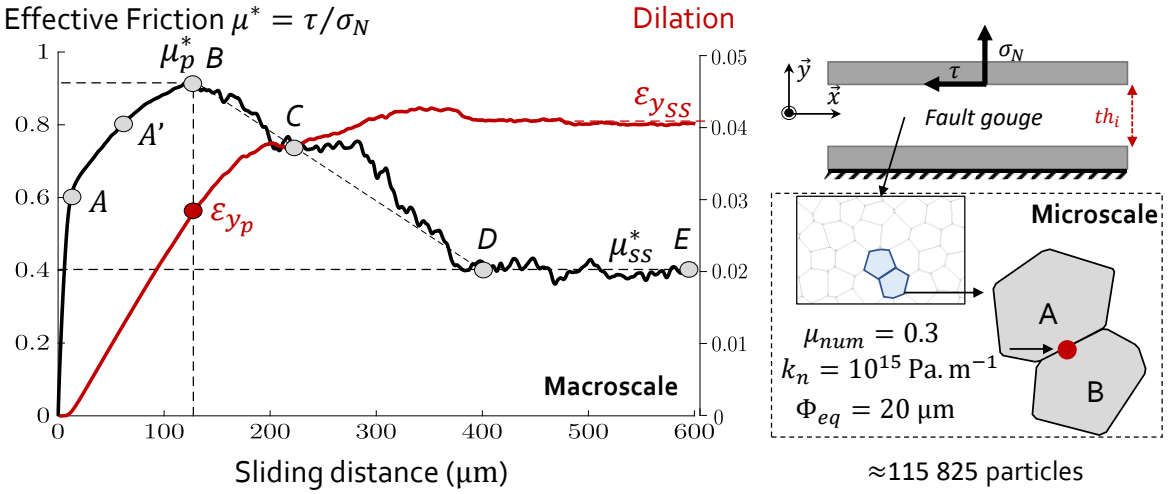

Figure 2. Effective friction μ^*(black curve) and dilation ε_y (red curve) as a function of the slip distance (μm) of the upper rock wall for the reference case (M-S). A is the end of the elastic zone. The zone from zero to B describes the pre-peak zone, followed by the slip weakening zone (B to D) and then by the steady-state zone (D to E). ε_{y_p} represents the critical dilation, i.e. the dilation at friction peak. It is also important to note the difference between the effective friction peak μ_p^* (maximum effective friction) and the steady-state effective friction μ_{ss}^* which is the average value of the effective friction once the plateau zone is reached and for a constant applied shearing velocity. The effective friction is not to be confused with the Coulomb-Mohr friction coefficient μ_f, or the interparticle friction μ_{num}.

Four main zones are highlighted with direct shear, Figure 2 & Figure 3, consistent with the main stages of Riedel shears formation (Marone, 1998). A pre-peak zone is first observed, composed of an elastic phase (0-A) allowing to define the shear modulus of the gouge. As dilation has not started yet, no significant volumetric deformation is observed within the gouge. Once the elastic zone is over, the sample is deforming in a non-reversible way until the friction peak (A-B), for which the maximum shear strength of the gouge is reached (B). During all this zone, the sample dilates (red curve), with a critical dilation ε_{y_p} still lower than the averaged steady-state dilation $\varepsilon_{y_{ss}}$. Riedel shear bands appear, following closely what is commonly observed in natural faults (Katz et al., 2004): primary R-bands R_3, R_4, and R_5, are first activated just before friction peak, and followed by secondary R-bands R_1 and R_2 at effective friction peak, with slightly lower Riedel angle orientation α_i. During the slip weakening period, or post-

peak stage (B to D), the friction gradually decreases until it reaches a friction stabilization plateau and maximum dilation at D. In this zone, primary R-bands are de-activated in favor of the two mains secondary R-bands R_1 and R_2, which localize all the gouge deformation (Figure 3). A boundary shear Y_1 also starts growing at the top of the gouge layer propagating from one R-band to another. In fact, it can be identified that the softening part between C and D corresponds to this propagation: going progressively from a fully coupled Y-band to a fully sliding Y-band, which causes this softening (*Movie S1*). Once the steady-state zone is reached (D to E), the gouge reaches a stationary state of evolution. The friction then fluctuates very weakly around a mean value which is similar in most of the simulations and ranges between 0.4 and 0.5. From this moment, the dilation of the granular sample is maximum and stabilized. In this regime, the main R-bands do not evolve anymore, a secondary Y_2-band is partly observed at the bottom rock wall, and the Y_1-band is fully formed at the top rock wall (D) and accommodates all the relative velocity (*Movie S2*).
Conjugate Riedel bands R' are also observed in the simulations, oriented at about $\alpha' \approx 60°$ from the top wall, a higher angle than for simple tensile T-bands (oriented in the direction of the major principal stress at 45°), but lower than that described for R'-bands observed in the literature, which approaches $75°$ [(Davis et al., 2000), (Katz et al., 2004)]. It is assumed that this is a rotation of the T-bands tending towards R-bands. Moreover, the theory of Riedel bands is based on the Coulomb-Mohr model, which is an idealized model that does not consider the post-peak decrease of the shear resistance. It is thus considered that the bands observed between 50 and 60° are indeed R'-bands according to their link with the observed Riedel structures.

The shapes of the Riedel bands observed are also interesting to study as they are most of the time not really linear and present some lower angle at the boundaries, as found by (Hirata et al., 2017). This can be partly due to the influence of boundary conditions.

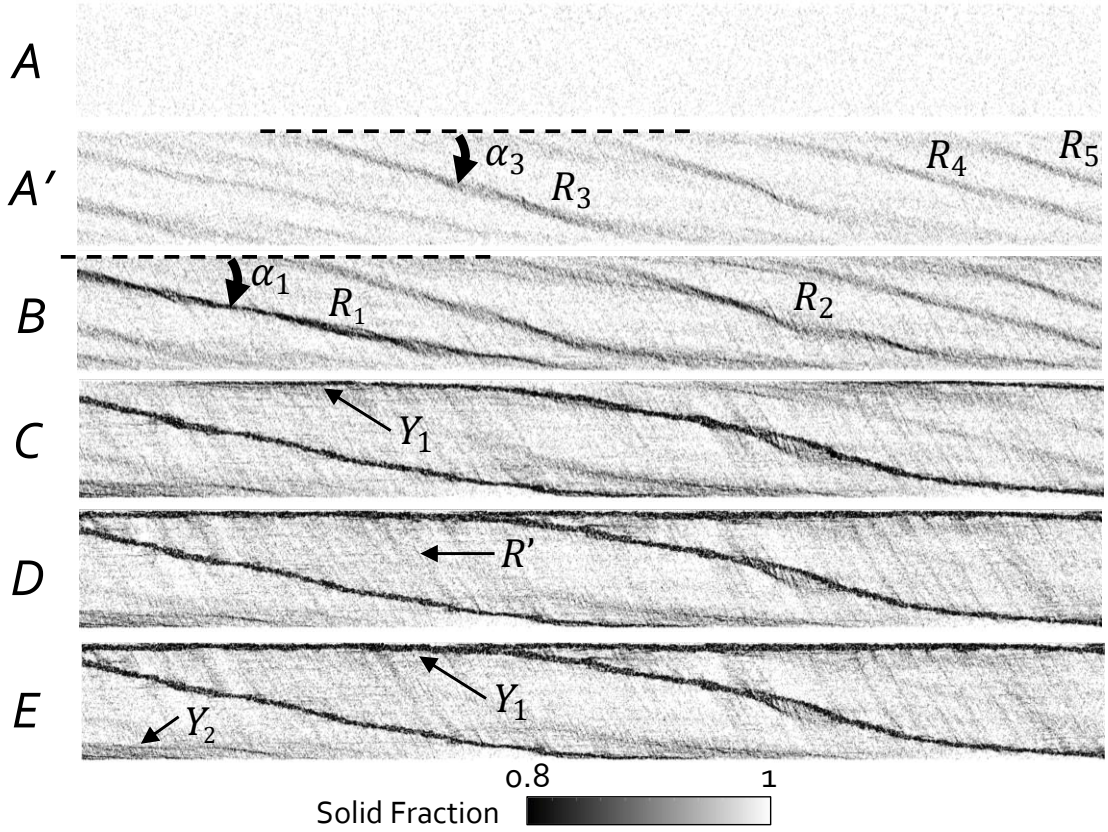

Figure 3. Solid fraction snapshots for reference sample (M-S). The solid fraction is used here to observe the rheology and deformations within the granular gouge. It is the ratio between the total surface of particles on the total surface of gouge (particles and voids). In the present case, it is plotted as a field, i.e. each pixel corresponds to the value of the solid fraction in its close neighborhood. The solid fraction is plotted between 0.8 and 1. Letters correspond to different steps in the effective friction curve in Figure 2. R_1 and R_2 are secondary *R*-bands, $R_3, R_4,$ and R_5 are primary *R*-bands, orientated at angle α_i from the direction of shearing. R' are conjugate Riedels orientated at angle α_i' from the direction of shearing. *Y* is the slip localization at the boundary: Y_1 is the main localisation zone occupying all the slip surface and Y_2 is a partially-developed boundary zone at the opposite surface. (*Movie S1*)

3.2. Link between particles characteristics, friction, and rheology

To characterize this matrix material, series of parametric studies were performed, varying geometrical (shape, size) or physical (interparticle stiffness and friction) properties of the matrix to represent different rock lithologies. These studies were done not only to observe the influence of each parameter on the mechanical behavior but also to observe how each characteristic is linked to the rheological behavior through Riedel band formation and evolution. All these lithologic variations are summarized into only three parameters: the interparticle friction μ_{num} (microscale), the effective shear modulus $G = \tau/\gamma$ (at the macroscale, the ratio between the shear stress τ and shear strain γ in the elastic regime), and the ratio of gouge thickness to grain size n_p (i.e. number of particles within the gouge thickness).

3.2.1. Interparticle friction controls Riedel shear bands orientation

A change in interparticle friction coefficient from 0.1 to 0.6 yields significant augmentation in effective friction peak values, and a small increase in the steady-state effective friction as shown in Figure 4 (a). Preliminary results had been shown in this sense (Casas et al., 2021). The slip weakening behavior thus evolves from a smooth (low μ_{num}) to an abrupt friction weakening (high μ_{num}), prone to switch the fault behavior from a ductile and aseismic slip to a more brittle and seismic one, Figure 5 (ii). An evolution in the interparticle friction between particles also drastically increases the orientation angle of the main Riedel bands from the beginning of the simulation and until steady-state, ($\approx 6\,°$ for $\mu_{num} = 0.1$ and $\approx 16\,°$ for $\mu_{num} = 0.6$), Figure 4 (b) and Figure 5. This is a typical result of Coulomb-Mohr's theory [(Tchalenko, 1970), (Katz et al., 2004)]. (Gu & Wong, 1994) plotted the evolution of Riedel angles α_i as a function of effective friction and also found an increase in α_i with the increase of internal friction angle. The theory requires an angle equal to $\alpha_i = \varphi/2$ for direct shear (φ internal friction angle), but the value of φ can be questioned: should it be the one of the peak, or the one of the plateau? The former seems inaccurate as numerical values of α_i are smaller than theoretical ones (which should be equal to 21.5° for the (M-S) case, *Table S2*). The latter does not work either, because the plateau is at the same friction coefficient for all cases, whereas the α_i values can vary a lot. It therefore appears that α_i is not only a material property, but also a structural property.

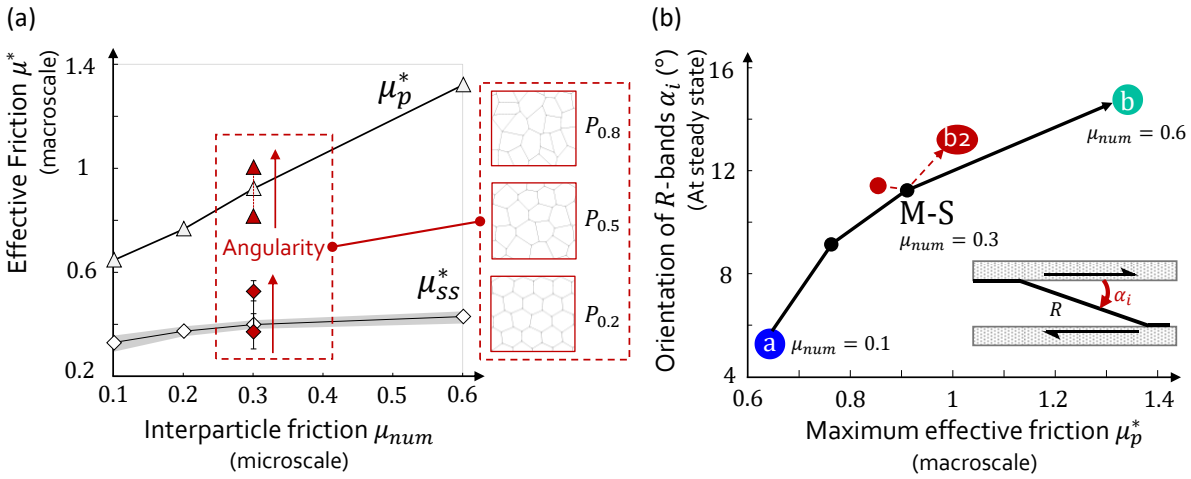

Figure 4. (a) Effective friction at peak μ_p^* and steady state μ_{ss}^*, as functions of inter-particle friction. And the effect of an increase in particles angularity (in red) ; (b) Orientation angle of Riedel bands α_i as a function of the effective friction peak for a variation in interparticle friction (black curve), from (a) to (b), or of the angularity of particles (red curve). Letters a, b, and b2 refer to Fig.5 for gouge kinematics.

Increasing interparticle friction also seems to increase the number of Riedel bands formed during shearing, resulting in a reduced average distance between two successive bands. These results are consistent with [(Lefevre et al., 2020) & (Jiao et al., 2021)] who reproduced sandboxes with different widths and found a link between the internal friction angle and the distance between Riedel shears.

An evolution of Riedel structures, i.e. the combination between Riedel bands and conjugate Riedels ($\gg 45\,°$ from the horizontal shear direction), is also observed at steady-state for a low μ_{num}, while only low Riedels are observed with increasing μ_{num}, Figure 5. However conjugate

Riedels are also more pronounced with higher friction during the weakening part. We carried out a similar study by slightly changing the shape of particles, giving more or less regularity and therefore more or less angular polygons, Figure 4 & Figure 5. The results are consistent with [(Mair et al., 2002), (Nouguier-lehon et al., 2003)] and show that the increase of angularity increases the resistance to friction, and thus the effective friction peak. Moreover, the angularity of particles seems to be quite important in the development of Riedel shear bands (Figure 5 b (b2)). In the same way as interparticle friction, a higher angularity P_i (similar to more disorder in the grain shape) results in a larger number of Riedels at friction peak. They are also less marked and of lower thickness. The change of angle orientation at steady-state is very small, meaning that the angularity of particles is too small to have a major influence on Riedel's angle orientation.

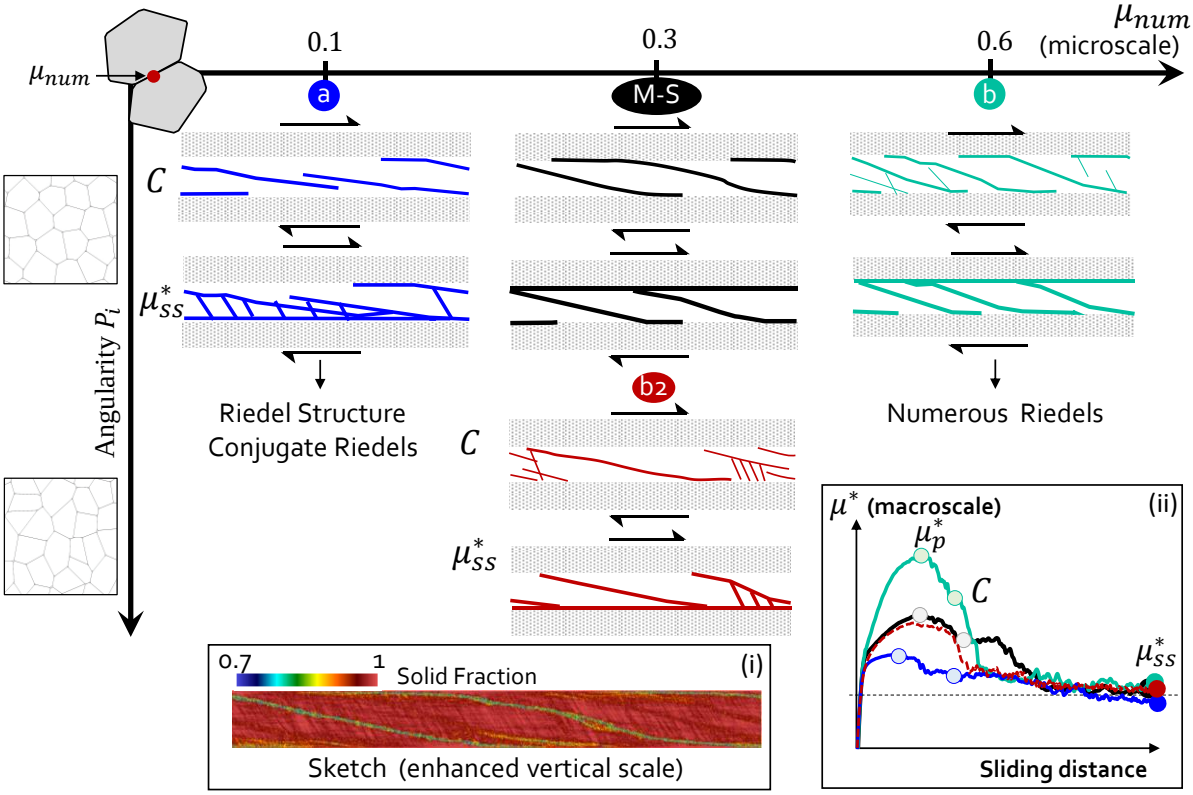

Figure 5. Riedel patterns as a function of the interparticle friction (horizontal axis) and the angularity (vertical axis), during the weakening part (C), or at steady-state (μ^*_{ss}). (i) Initial solid fraction for sketches – Reference case (M-S) at point C. (ii) Effective friction as a function of the sliding distance for the four different cases.

3.2.2. Gouge shear modulus influence on Riedel structure

It is interesting to mention that an increase in the interparticle stiffness (purple in Figure 6) and an increase in the particle size (orange in Figure 6) both lead independently to an increase in the shear modulus, *Figure S4*. This augmentation of shear modulus increases the effective friction peak, Figure 6 (a), and the total energy released during the weakening phase, Figure 6 (b). A modification of the interparticle stiffness k_n manages the type of material behavior. Concerning the grain size effect, it is clearly a modeling artifact: a sample with large grains is simply stiffer because the number of elastic accommodation sites (interparticle contacts) is

reduced while their compliance is constant, thereby artificially stiffening the granular assembly. It also appears to change the number of particles within the gouge thickness, which also affects gouge behavior. In the remainder of the paper, we will only deal with the increase in shear modulus data coming from an increase in the contact stiffness between the particles.

Comparing two different shear modulus (M-S) and (g), the pattern of the friction curve was predictable for the elastic part, as numerical stiffness is only supposed to play on the overlapping of particles which controls the elastic part of the effective friction curve: an augmentation in interparticle stiffness increases the global stiffness, and thus the shear modulus.

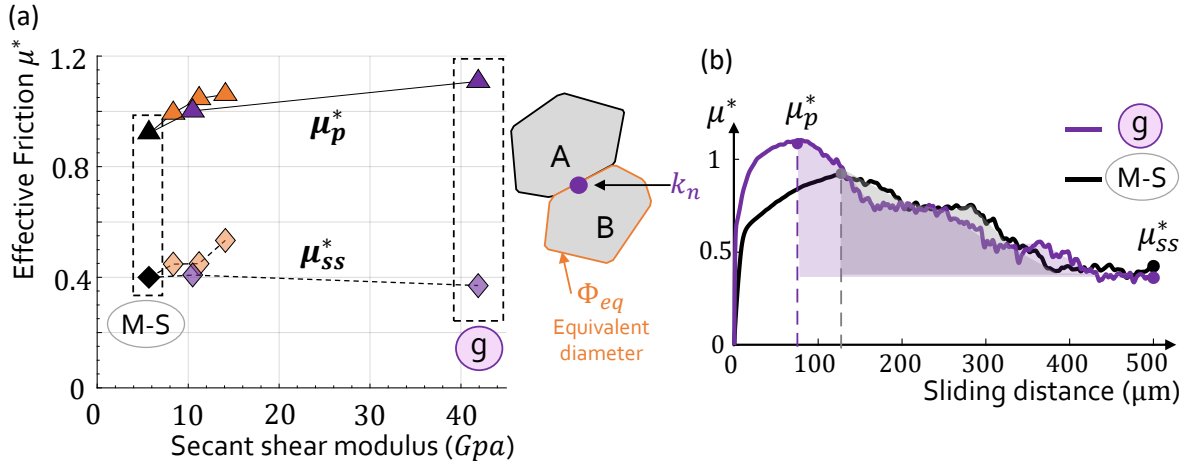

Figure 6. (a) Effective friction as a function of secant shear modulus (GPa) for friction peak μ_p^* and steady state friction μ_{ss}^*. The increase in shear modulus corresponds to an increase in interparticle stiffness (purple points, 10^{15} Pa/m, 2 10^{15} Pa/m and 10^{16} Pa/m) and to an increase in the size of particles (orange points, 20 μm, 30 μm, 40 μm, and 50 μm with the same interparticle stiffness of 10^{15} Pa/m. Details on shear modulus calculation and values are in (*Figure S3 and Table S3*). (b) Effective friction profile of gouge (M-S) and gouge with an increase in shear modulus (g).

How does shear modulus affect Riedel band formation? Figure 7 presents simulation snapshots of Riedel shear bands for the reference case and the maximum shear modulus obtained (patterns for an increase in stiffness, (g) letter in Figure 6). The orientation angle of the main Riedel band α_i is reduced from 12° to 7°. From friction peak to steady state, the increase in G completely changes the kinematics inside the gouge, Figure 7 (a) & (b). The gouge material (g) has a single final R-band that runs the length of the gouge and appears to have two slopes with different orientations. A Riedel structure is formed with many conjugate Riedels, Figure 7 (b), as opposed to the reference case (M-S) counting with only two secondary Riedel shear bands. Hence, an increase of shear modulus not only leads to a decrease in the angle orientation of the main Riedel bands but also to the formation of a complex Riedel structure. Figure 7 only shows the case with the highest shear modulus, but the intermediate cases show a progressive evolution of the rheology from the reference case (M-S) to the case (g). More results can be found in (Casas, 2022).

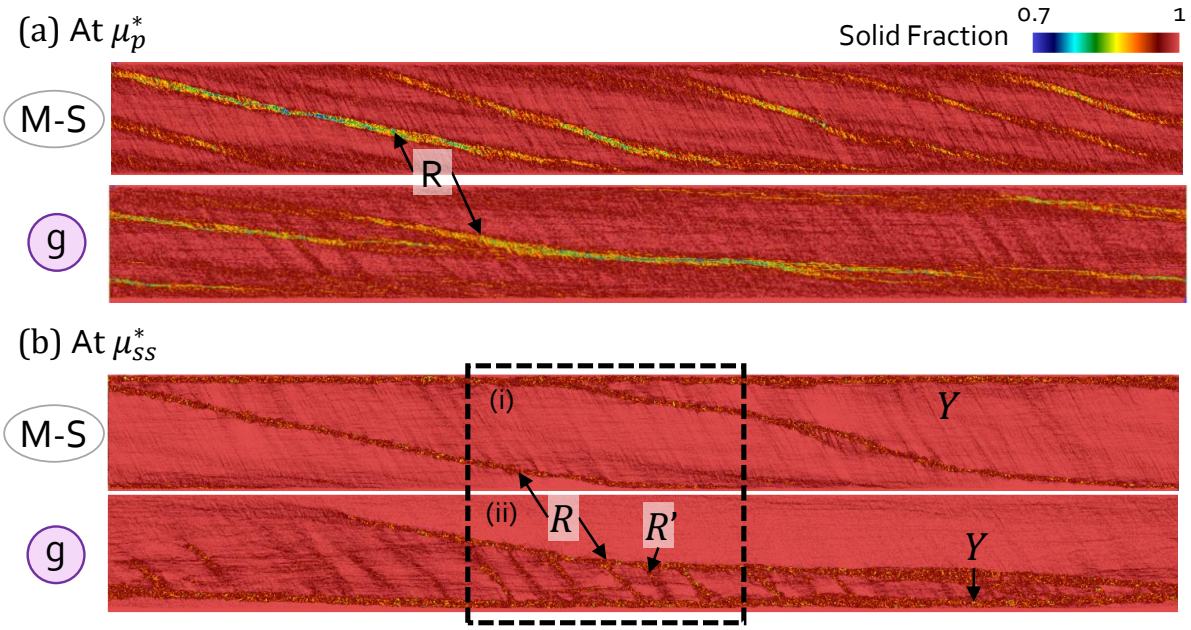

Figure 7. Solid fraction between 0.7 and 1 for the two samples (a) at effective friction peak μ_p^* and (b) at steady-state μ_{SS}^*. For an increase in shear modulus, the *Y*-localization occurred on the lower part of the gouge, as the entire upper part moves as one unit, unlike the (M-S) material which localizes at the top, due to the left Riedel band which only allows part of the gouge to move along the *x*-axis.

Conjugate Riedel shear bands, *R'*-bands, are rarely observed because of their short lifespan and limited thickness. They rotate at a higher speed than the *R*-bands and usually disappear as they grow [(Morrow and Byerlee, 1989), (Logan et al., 1992), (Morgan & Boettcher, 1999)]. That is why in several studies [(Schmocker et al., 2003), (R. Katz et al., 2006)], the *R*-bands are the only bands observed. In this study, conjugate Riedel bands *R'* are very pronounced in the case of the highest shear modulus. These R'-bands are present during the whole simulation and seem to be responsible for the difficulty of the material (g) to deform by shearing, inhibiting multiple *R*-bands formations. The distribution of force chains in the two types of gouges, Figure 8, allows us to better understand the formation of R'-bands. In both cases the total transmitted force is similar, but the transmission of forces goes through different paths. In areas without Riedel, the material is very compacted and the force transmission is diffuse (i.e. continuum-like). Within Riedels, where the localization of deformation takes place, the material is granular with high porosity, so force chains are very localized, forming a rather discrete network. On the other hand, the junction between the different bands are places of stress concentrations, reflecting kinematic incompatibilities. It can also be noted that the observed thickness of conjugate Riedels is thus linked to the magnitude and width of the force chains network: conjugate Riedels will have a higher thickness (more visible) for stiffer or stronger materials with a higher magnitude of force chains. An overview of force chains within the material can therefore help to characterize the different types of deformations related to the two types of Riedel bands.

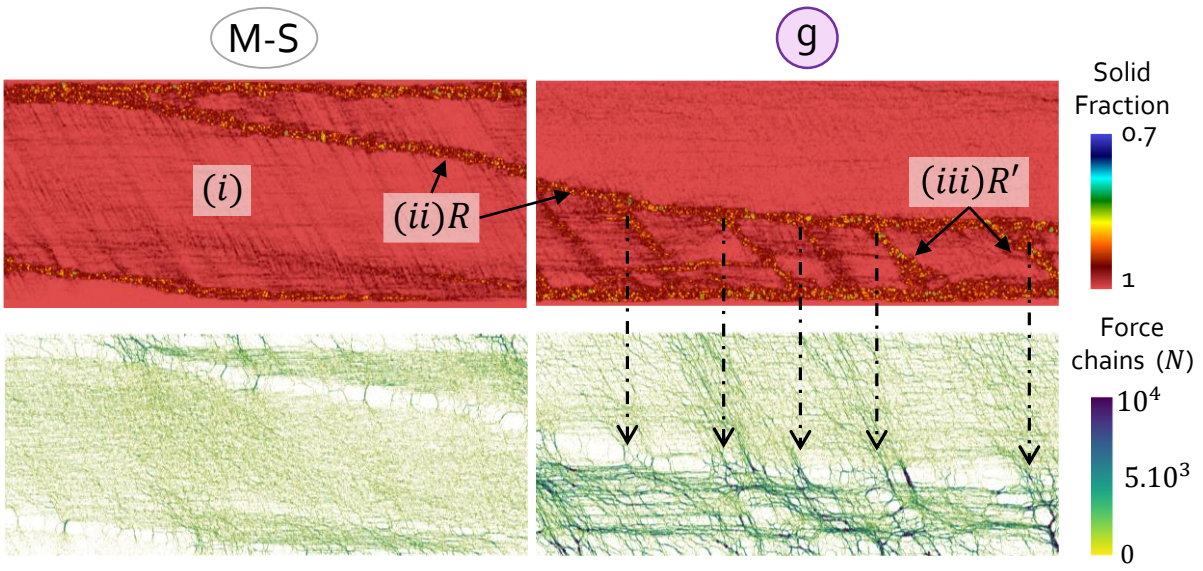

Figure 8. Zoom in on Figure 7 (b). The solid fraction is shown between 0.7 and 1 and a snapshot of force-chains networks is plotted from 0 to 10^4 N. Force chains are defined according to the typical level of stress present in the system (here the applied normal stress) and thickness and color are evaluated between the minimum and maximum contact force (0 to 10^4 N). A cut-off is made at 10^4 N to have the same visualization for all cases (higher force chains are observed for higher stiffness).

3.2.3. Role of the number of particles within the gouge thickness

Figure 9 presents the angle orientation of the main Riedel shear band α_i as a function of the number of particles in the gouge thickness n_p, which is also the ratio between gouge thickness and size of particles. Hence, a change in n_p is tested by changing two parameters: a modification in the initial gouge thickness with the same size of particles (green), and an increase in the size of particles, with the same initial thickness and with a corrected stiffness effect (blue, keeping the shear modulus constant).

A modification of n_p alone has no important influence on the shear modulus, nor on the observed effective friction, (*Figure S5*). However, a link is found between n_p and the type of Riedel structure formed. Reducing the number of particles in the thickness tends to favor the formation of a Riedel structure composed of many conjugate Riedels and for which the orientation of Riedel bands is lower, Figure 9 (c) & (e). This confirms that the orientation of Riedel bands is not only a material property but also depends on other fault properties. Some very thin gouges were also modeled with extremely low $\boldsymbol{n_p}$ ($th_i = 200\ \mu m$, 10 particles), and it was found that a minimal n_p (around 10-15 particles) is necessary to observe any slip localization and deformation in our simulations. Below this number, bulk shearing of the whole gouge is observed. This low number of particles can be related to a very young fault where few wear particles would still be formed (Scholz, 1987). On the other hand, a very large n_p favors a multiplication of Riedels with a higher orientation angle. This result was only partially discussed in the literature, in the sense that particle size evolution was found to be responsible for the R-band angle as well as the gouge thickness, but the link between these two parameters was less investigated. When increasing the initial gouge thickness, a change in orientation is observed close to the boundaries, which may come from effects due to the larger sample.

Besides, fault gouges with an identical number of particles within the gouge thickness, and no variation of shear modulus will show the same slip behavior (effective friction and deformations), *Figure S6*.

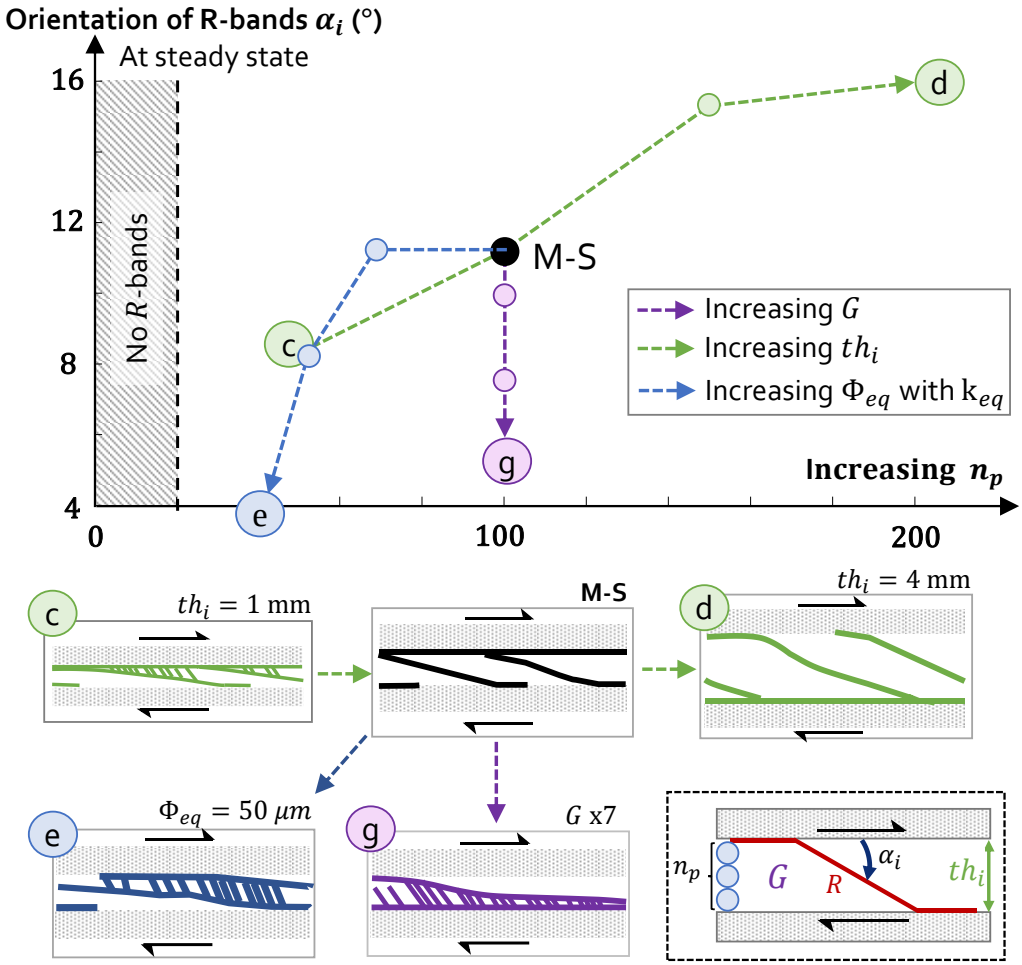

Figure 9. Schematic view of the angle orientation of the main Riedel shear band α_i as a function of the ratio n_p, with distinction between 3 increasing parameters: (c) to (d) increase in the gouge thickness th_{pi}, (M-S) to (e) increase in the size of particles $\Phi_{eq}$with corrected contact stiffness $k_{eq}$to keep the same shear modulus for each gouge, (M-S) to (g) increase in the shear modulus G. The sense of the arrow represents an augmentation of all the parameters previously presented as detailed within the legend. Riedel structure patterns are represented below the figure and correspond to the extreme cases of the numerical campaign at steady-state. Details on Shear modulus values can be found in *Table S3*.

3.3. Slip weakening and breakdown energy

In the proposed models the sliding is imposed by artificial boundary conditions (imposed slip velocity), and therefore cannot be claimed to be realistic. In seismic faults, the sliding is driven by the elasticity of the surrounding medium, and can therefore take place in a stable or unstable way, and involve the existence of a propagating front. The models used here are local micromechanical studies of the behavior of fault gouges, which are designed to be inserted in larger-scale dynamic models. But to have a broader understanding of these mechanisms our results are interpreted through slip weakening models.

The well-known critical distance D_c is the slip distance corresponding to a drastic decrease in frictional strength (Rabinowicz, 1951), and is considered to be the distance necessary for the renewal of the contact surfaces (Dieterich, 1979). We can thus define the slope of friction drop or weakening rate (in Pa/m) as follows

$$K_c = \frac{\left|\mu_{ss}^* - \mu_p^*\right|}{D_c}\sigma_N \tag{1}$$

Slip instabilities may occur if the loading stiffness of the fault K (i.e. stiffness of the loading system) appears to be lower than K_c ($K_c > K$). The linear fitting of the weakening part of the effective friction curve may however induce errors because this weakening is sometimes rather far from being linear. We, therefore, adopt a different approach to determine it. This weakening slope is indeed very much related to the breakdown energy released during the slip. In our model, E_B can be calculated as the area under the friction-slip curve, corrected by subtracting the steady-state friction, and will lead to the extraction of the weakening slope, Figure 10 (i):

$$\left(\tau_p - \tau_{ss}\right) * \frac{D_c}{2} \equiv E_B = \int_0^{D_c^+} (\mu^*(U) - \mu_{SS}^*)\sigma_N \, d_U \tag{2}$$

Where $(\mu^*(U) - \mu_{SS}^*)\,\sigma_N$ is equal to $(\tau(U) - \tau_{SS})$, where D_c^+ is any sliding distance larger than D_c (this can be checked afterward), and where the lower bound of the integral corresponds to the instant of the peak, from which Dc is considered. D_c is therefore inverted from the peak and steady-state frictions and from the breakdown energy required to slide from the former to the latter.

As observed in section 3.2, interparticle friction has a large impact on the K_c value, Figure 10 (a), while its influence on breakdown energy is not so important compared to other variations, Figure 10 (d). A higher increase in E_G is observed when decreasing n_p with the opposite effect on K_c, Figure 10 (f) and (c). A high value of initial tangent shear modulus increases both K_c and E_G, although its influence is less important than n_p or μ_{num}, Figure 10 (b) and (e). An increase of K_c (even for a low energy) can be quite influential as it also implies a reduction of the sliding distance necessary to weaken the fault, which could tend to more sudden slips and therefore to an unstable sliding. These results agree with the Riedel structure observed in section 3.1: materials with low K_c present lower Riedel angles and a highly visible Riedel structure, promoting slip stability (high D_c).

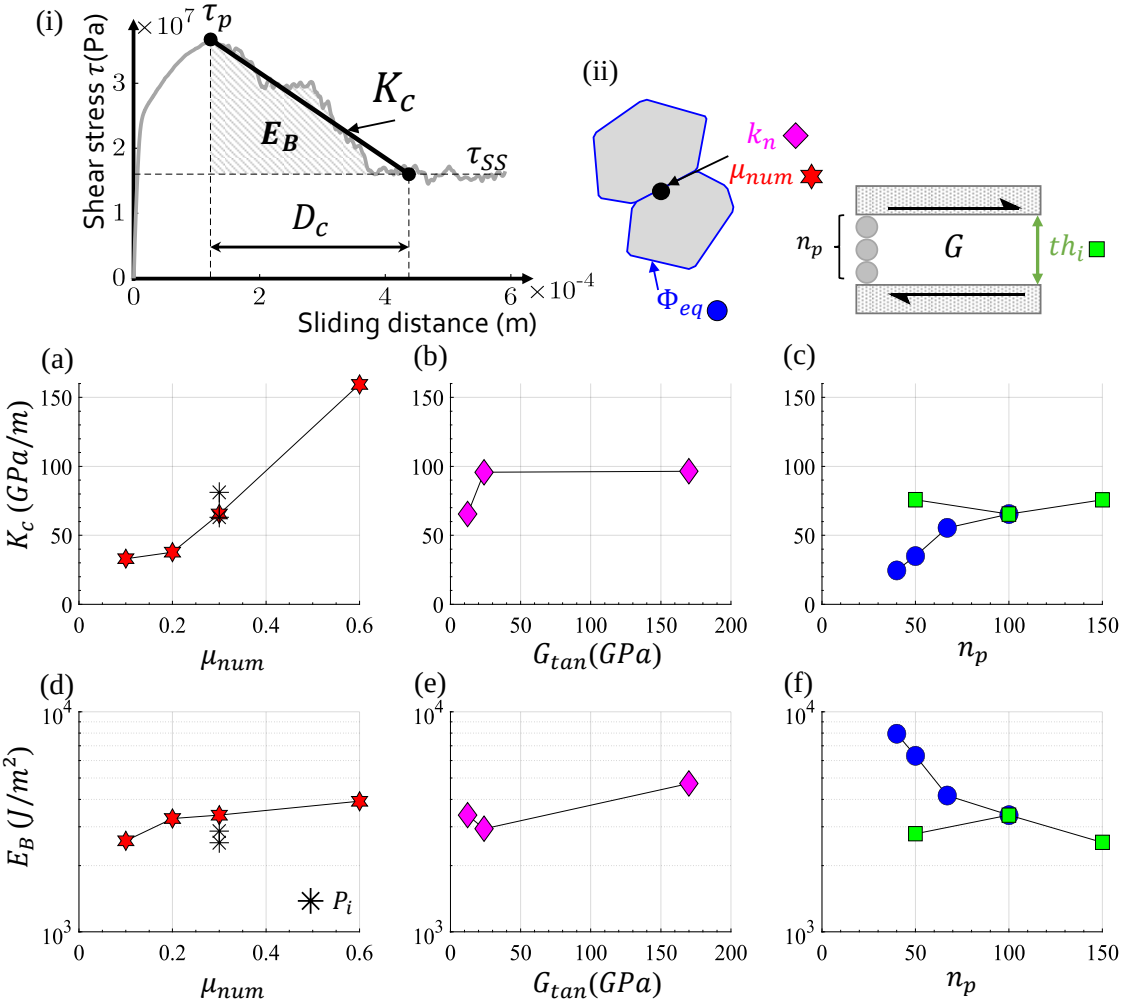

Figure 10. (i) Reference sample (M-S) results where the shear stress variation (Pa) is observed as a function of the slip distance (m). The slope K_c is calculated to have the same energy in J/m^2 for the triangle generated by the slope line than the E_B (colored in grey). With τ_p the maximum shear stress (Pa), τ_{ss} the dynamic (or steady-state) shear stress (Pa) and D_c the critical slip weakening distance (m). In this figure K_c fits well with the shape of the decreasing shear stress, but it is not as satisfactory for all the models tested, Figure S6. (ii) legend with color-coded shapes; Evolution of the critical weakening slope as a function of the (a) interparticle friction, (b) the initial tangent shear modulus G_{tan}, and (c) number of particles within the gouge stiffness. Evolution of the breakdown energy as a function of (d) the interparticle friction, (e) the initial tangent shear modulus, and (f) the number of particles within the gouge stiffness. Each graph represents the influence of a certain variable on the evolution of K_c ou E_B, but we have only shown the data that changes with the indicated abscissa.

4. Discussion on gouge rheology and slip weakening

4.1. Link between gouge characteristics and Riedel bands patterns

A small change in gouge characteristics impacts Riedel shear bands formation through their orientation angle α_i and the type of Riedel structure formed. It is interesting to note that all the tested parameters influence α_i in a certain way, meaning that Riedel shears are not only linked to the external loading conditions but also depend on internal fault gouge properties. As previously highlighted, three relevant quantities control the principal orientation angle of *R*-bands at steady-state: the interparticle friction μ_{num}, the number of particles within the gouge

thickness n_p, and the effective shear modulus G. Figure 11 presents the angle orientation of the main Riedel shear band α_i as a function of the effective friction peak, for all the studied cases compared to the standard case (M-S) described in section 3.1.

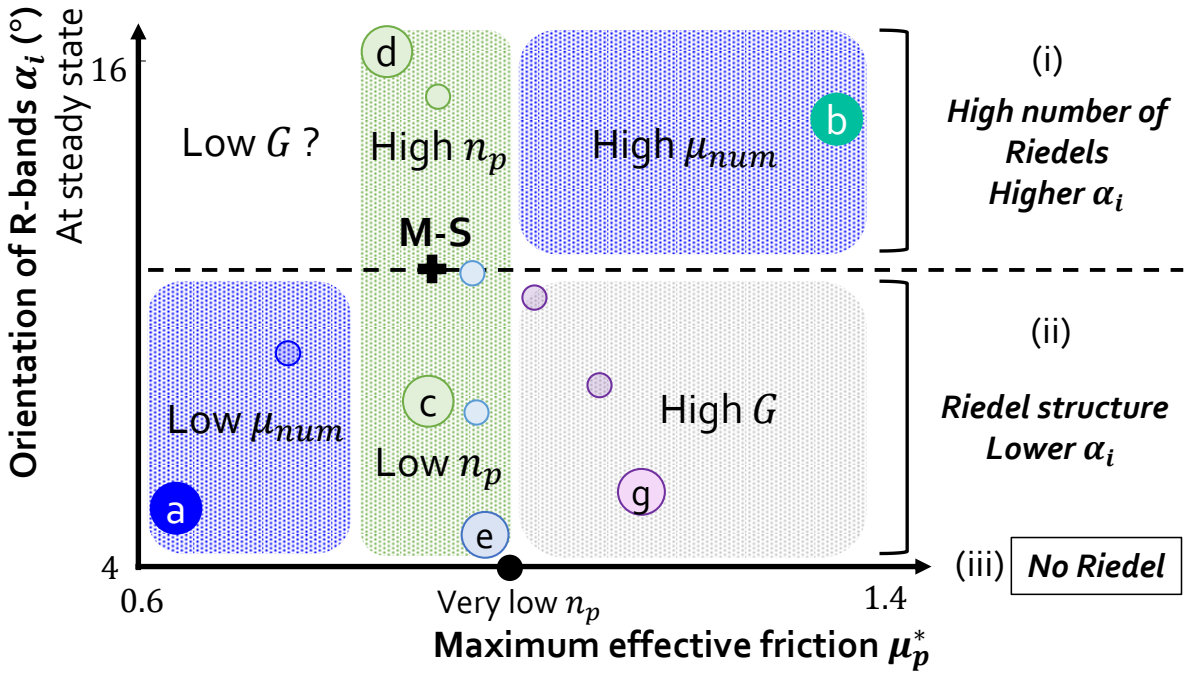

Figure 11. Schematic view of the orientation of *R*-bands α_i at steady-state as a function of the effective friction peak μ_p^*, with distinction between six major zones of interest: reduction or increase of interparticle friction μ_{num}, reduction or increase of n_p (without modification of the shear modulus) and reduction or decrease of the effective gouge shear modulus G. This graph only presents the Riedel patterns at steady-state because α_i variations with other instant of the simulation are not very significant ($\sim 1-2$ °). These variations were not studied in the present study but could be monitored at a different moment of the simulation (elastic phase, effective friction peak, weakening part…) in future research work.

Figure 11 zone (i) gathers fault gouges with a high μ_{num} or a high n_p. These parameters increase the orientation angle α_i of Riedel bands and the number of Riedel shear bands appearing during the simulation (from effective friction peak to steady-state). By **increasing only μ_{num}** (ex. due to mineral transformation, chemistry, surface, and grain shape roughness), both the maximum shear stress, and thus μ_p^* are increased without changing the shear modulus. A reduction of the critical slip distance is observed, leading to a more sudden post-peak weakening, which is prone to switch the fault behavior from a ductile aseismic response to a brittle seismic slip, depending on the stiffness of the surrounding medium. Materials with high interparticle friction coefficient (and low stiffness) are also known to present greater slippage and a decrease in the recurrence time between two slip events (Dorostkar & Carmeliet, 2019). At constant grain size, increasing the gouge thickness automatically **increases n_p.** Interpreted in terms of real fault, these n_p variations correspond to different locations within the sliding zone, but not to the evolution of the same sliding gouge part (since it would imply wear or a reduction of the size of certain particles in the center of the sliding zone). For these materials μ_p^* slightly decreases and the orientation angle of Riedel bands increases. According to (Scholz

et al., 1972), an accumulation of gouge layers tends to stabilize the system, and according to (Moore & Byerlee, 1992)'s theory, small Riedel angles also tend to stabilize the system. In our case, it seems that we have two competing effects: an increase in both the thickness of the gouge layer and in the orientation angle of the R-bands. These results could also be related to the stick-slip phenomenon obtained by (Lyu et al., 2019) when testing a variability of gouge thickness with different normal stresses. They observed that an increase in layer thickness, (i.e. an augmentation of the number n_p) implies a reduction of stress drop and friction and has a significant effect on stick-slip. On the top left of the graph we notice an area without measurement points. Following the logic of the graph, we suppose that it corresponds to fault gouges with a very low shear modulus. This result remains to be verified with future simulation or experimental results.

Conversely, Figure 11 zone (ii) gathers fault gouges with a low μ_{num}, a low n_p, or a high G. For these materials, a similar rheological behavior is observed with a decrease in the orientation angle α_i of Riedel bands and the presence of a well-formed Riedel structure at steady-state (Riedels and conjugate Riedels). The mechanical or physical changes applied to the fault gouge enhance the lifespan of R'-bands in their maximum size, explaining why more Riedel structures are observed, which may also increase the critical weakening length. However, their consequences on gouge strength and breakdown energy lead to different types of sliding behavior. Materials with **low $\boldsymbol{\mu_{num}}$** show a reduction in the maximum effective friction. From the point of view of (Moore & Byerlee, 1992), they are prone to enhance stability within the gouge sample by reducing the stress drop. They can be related to weak gouges behavior [(Collettini et al., 2019), (Bedford et al., 2022)] which are supposed to have a very small effective friction. As opposed, materials with **high $\boldsymbol{G}$** produce a higher resistance to slipping. The stiffness of the fault was found to depend on the ratio of the shear modulus to the size of the rupture nucleation zone (Leeman et al., 2016). A reduction in the $\boldsymbol{n_p}$ is not necessarily linked to an increase in shear modulus, and the effective friction peak μ_p^* is almost no affected.

For very "young" fault gouge with a very thin granular layer (extremely low $\boldsymbol{n_p} \ll 10-15$), and for any combination in the other gouge characteristics, Riedel bands formation is prevented, Figure 11 (iii). The maximum shear stress also increases whereas the dilation is slightly reduced, as previously found by (Biegel et al., 1989) for a reduction in fault gouge thickness. This means that in order to observe shear localization in fault gouges, they must be mature enough to have a sufficiently thick and comminuted gouge to allow Riedel localization.

4.2. Occurrence of dynamic slip instabilities

Even though K_c can be extracted from each model, the difficult question remains: what is the stiffness of the crust, and to what quantity should the shear stiffness be compared? In laboratory experiments, it should be the stiffness of the loading apparatus, but for numerical experiments, we don't have such a value to consider. From crack theory, the global loading stiffness K is defined by the ratio of stress to displacement. The fault stiffness K is found to be proportional to the ratio G/L, with G the shear modulus and L the length of the slipping fault section, meaning that the loading stiffness decreases as the slipping fault section increases, Figure 12

(a). If the slipping region is treated as an elliptical crack (Scholz, 2002), the critical nucleation length before dynamic slip instabilities L_c can be calculated as

$$L_c = \frac{E}{2(1-\nu^2)K_c} \tag{3}$$

With E a relevant young modulus (or equivalent elasticity modulus), ν the Poisson ratio and K_c the critical weakening slope. The fault is supposed to be unstable when the slipping fault section L exceeds the critical nucleation length L_c. Figure 12 (b) illustrates the dynamic behavior observed when L_c is reached, with a sudden transition from the nucleation to the unstable phase.

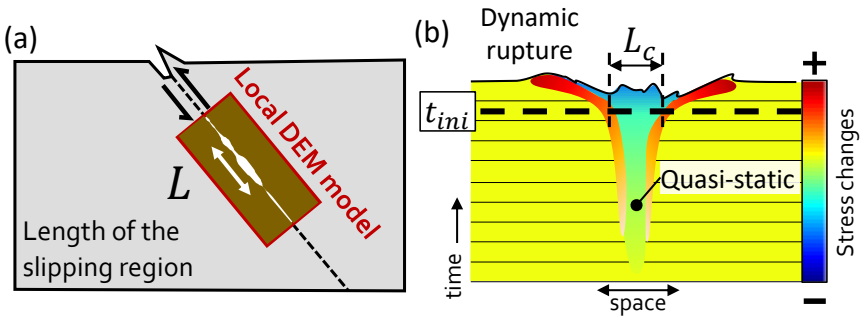

Figure 12. (a) A schematic figure showing the nucleation length L on a frictional fault plane. (b) Initiation of dynamic rupture from a smooth nucleation model, (figure redrawn from (McLaskey, 2019)).

From our numerical data, we can use Eq. (3) to extract the nucleation length L_c. The objective here is not to predict the "exact" value of L_c, but to observe trends and to put forward a dependence of L_c on certain gouge characteristics. The linear slip weakening approximation allows us to identify certain slip behaviors and link them with the previously observed rheology of gouges. At a first glance, the nucleation length is observed to evolve linearly with the increase of the breakdown energy, Figure 13 (a). Around this trend, several outliers deserve to be mentioned. The area (i) gathers simulations performed with low inter-particle friction, they result in a higher L_c than the standard case (M-S) and a rather low breakdown energy E_B. In this case, there is much more mobility within the fault due to the large distance of slipping before dynamic slip instabilities happen. When n_p is reduced, in zone (ii), the observed breakdown energy E_B increases as well as the critical nucleation length L_c. The mechanical behavior is similar to the one of weak materials, but with a material that takes more time to stabilize over time, explaining the higher fracture energy observed. It also means that this long and smooth slip weakening decreases the probability of dynamic instabilities to occur, but that they will present a larger stress drop should they happen. These two cases showed Riedel structure at a steady state of sliding. In zone (iii), fault gouge materials with high G or high μ_{num}, produce a higher resistance to sliding, giving a shorter nucleation length and medium breakdown energy value. A rather unstable behavior could be observed as a smaller slip is needed before dynamic slip instabilities happen. However, the link is still not clear between Riedel structures and dynamic slip stabilities because this zone (iii) presents different localization patterns at steady-state with a Riedel structure for a high G and only Riedels for high μ_{num}, despite the similar value for breakdown energy and nucleation length.

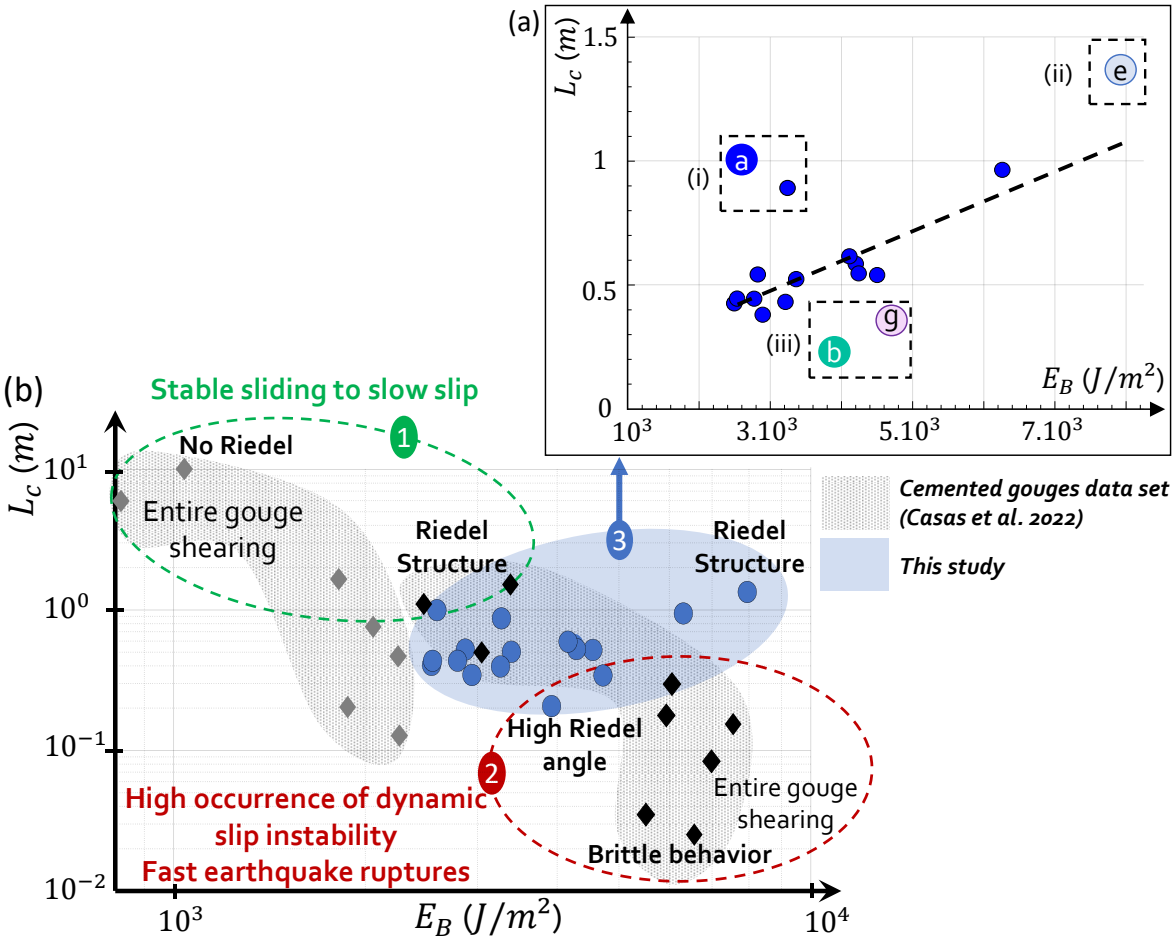

Figure 13. (a) Evolution of the critical nucleation length L_c (m) as a function of the Breakdown Energy E_B (J/m^2) for all the matrix simulations, linear-scale. (b) A larger picture of the L_c (m) as a function of E_B (J/m^2), log-scale, with results from (Casas et al., 2022) on cemented fault gouges with a variation of the percentage of cement for both dense (dark grey markers) and mid-dense samples (light grey markers). Matrix fault gouges of the present study are colored in blue. The choice was made to compare all the results using the same Young modulus and Poisson coefficient in Eq. (3) as if the same fault rock material was compared. Medium values for granite material are considered, $E \sim 60\ GPa$, and $\nu = 0.3$, with an approximate $K_{mean} \sim 900$ GPa/m (considering the $20\ mm$- length gouge). All these results come from numerical experiments.

The comparison of these results with previous studies on cemented fault gouges from (Casas et al., 2022) in the same Figure 13 (b) provides a more comprehensive view of the behavior of fault gouges. Both initial porosity and initial percentage of cementation influence gouge weakening and slip behaviors, playing a role in the gouge strength (brittleness, cohesion) and granular flow (particles agglomerates, Riedel bands). While the evolution of L_c with respect to E_G of matrix gouges is rather linear, the behavior of cemented gouges evolves in two steps depending on the initial porosity in the sample and the percentage of cement initially present in the numerical fault gouges. It is indeed clear from these revisited results that an increased porosity decreases E_B, and that an increased cementation decreases L_c.

– Fault gouges with high L_c ($\gg 1\ m$) and low E_B ($\ll 3.10^3\ GPa$), (green zone 1), correspond to loose materials, fault gouges with no or very few infill material (cement), or small inter-

particle friction. They present a low friction peak and weakening rate. These materials are close to those defined as weak gouge materials [(Orellana et al., 2018), (Collettini et al., 2019), (Bedford et al., 2022)] with a rather ductile behavior that tends to increase both the critical slip distance and the critical nucleation length. Greater mobility is thus allowed within the fault, and the associated breakdown energy remains low. They may lead to stable sliding or slow slip in the fault zone: very low shear modulus combined with large regions of nucleation is more likely to tend toward slow slip nucleation [(Leeman et al., 2016), (Scuderi et al., 2020)]. Regarding rheology, low cemented materials follow a rather ductile behavior without observation of apparent Riedel bands inhibited by a critical dilation higher than 1%, may the tested samples be dense and mid-dense. Their behavior is close to fault gouges with small interparticle friction presenting a Riedel structure with a very low Riedel angle orientation.

– A second domain, with low L_c ($\ll 0.5\,m$) and high E_B ($\gg 3.10^3\,GPa$), (red zone 2), gathers both dense and highly cemented fault gouges and matrix fault gouges from the zone (iii) previously described with high interparticle friction or shear modulus. They present a high friction peak and a high weakening rate. However, for these materials, the observed stress drop is much larger and also steeper (sharp, short, and intense peak), which means that if the shear stress peak is reached, the observed slip is more likely to occur in an unstable manner and with high energy release. The nucleation length decreases with an increase in cementation or interparticle friction, confirming that not much mobility is allowed within the system before the onset of dynamic instability, and increasing the risks of seismic instabilities to happen. Riedel bands are significantly affected by a change in contact laws between particles (cohesion or friction) occurring with cement breakage. They appear for dense materials when a threshold of cementation is reached and are directly linked to the importance of the dilation phase, [(Caniven et al., 2021), (Casas, 2022)] since the majority of the gouge remains cemented even after the weakening phase. Cementation and high interparticle friction play a major role in the triggering of instabilities and perhaps also in fast earthquake rupture behaviors.

It is clear from this picture that both internal characteristics of the fault gouge and infill materials have a very important role in the occurrence of dynamic slip instability, and this observation gives new considerations to the study of the different classes of slow earthquakes and fast earthquake rupture [(Leeman et al., 2015), (Bürgmann, 2018), (Passelègue et al., 2019), (Im et al., 2020)]. There is an evident link between mechanics (friction) and energy-related quantities such as L_c and E_G, but the link between *R*-bands and dynamic instability occurrence is still unclear. Although Riedel bands are not sufficient to detect unstable behavior, they are nevertheless a necessary condition (Moore et al., 1989), leading to the conclusion that dense and highly cemented materials are more likely to generate unstable behaviors, while mid-dense or dense materials with very low cementation will rather tend towards a ductile, and stable behavior. Next objectives will be to link the presence of a Riedel structure or conjugate Riedels to a characteristic increase or decrease of critical nucleation length and breakdown energy.

5. Conclusions

A set of 2D-DEM simulations was performed with numerical fault gouges composed of a very dense assembly of polygonal-shaped particles. The first aim was to explore the link between grain-scale gouge characteristics and fault gouge kinematics with shear bands formation during friction weakening. It was found that a small change in gouge characteristics such as the interparticle friction, gouge shear modulus or the number of particles within the gouge thickness impacts Riedel shear bands formation through their orientation angle and the type of Riedel structure formed. Moreover, in order to observe any shear localization in fault gouges, they must be mature enough to have a sufficiently thick and comminuted gouge to allow Riedel localization.

Then it appears that, even for similar rheological behaviors, different consequences can be observed on breakdown energy and the occurrence of dynamic slip instabilities. Fault gouges with low interparticle friction, (or with no or very few cementation), allow greater mobility within the fault and give low breakdown energy. They also present a decrease in the orientation angle of Riedel bands assumed to be characteristic of a more stable fault gouge. These materials lead to rather ductile behavior with low friction peak and weakening rate (weak gouge) and are expected to lead to a rather stable sliding or slow slip. On the contrary, materials with high interparticle friction or high bulk shear modulus**, (**or dense and highly cemented fault gouges), are less compliant materials. Not much slip is needed before going into dynamic slip instabilities, and high breakdown energy is observed. They present a high friction peak and a high weakening rate, which is prone to switch the fault behavior from a ductile aseismic response to a brittle seismic slip and increase fast Earthquake Rupture.

This study reinforces our convictions about the importance of Riedel shear bands within the fault, and the need to understand their link with the occurrence of dynamic slip instabilities. In the next step, we will focus on an energic method to link the behavior of each band of deformation with the friction observed in the gouge.

Acknowledgments

This study was funded by INSA Lyon, through a national Ph.D. grant led by A. Daouadji and G. Mollon. The authors declare that they have no competing financial interests.

Data Availability Statement

All simulations were performed with the open-source software MELODY version 3.94 (https://doi. org/10.5281/zenodo.4305614) developed by the second author and described in Mollon (2018). Simulation results can be found in Casas, Nathalie (2022), “Influence of grain-scale properties on localization patterns and slip weakening within dense granular fault gouges”, Mendeley Data, V1, doi: 10.17632/pphkhf72r5.1

Other explanations are included in the Supporting Information file or are available by contacting the corresponding author at nath27casas@gmail.com (Nathalie Casas).

References

Abercrombie, R. E., & Rice, J. R. (2005). Can observations of earthquake scaling constrain slip weakening ? *Geophysical Journal International*, *162*(2), 406–424. https://doi.org/10.1111/j.1365-246X.2005.02579.x

Aharonov, E., & Sparks, D. (2004). Stick-slip motion in simulated granular layers. *Journal of Geophysical Research: Solid Earth*, *109*(9), 1–12. https://doi.org/10.1029/2003JB002597

Anthony, J. L., & Marone, C. (2005). Influence of particle characteristics on granular friction. *Journal of Geophysical Research: Solid Earth*, *110*(8), 1–14. https://doi.org/10.1029/2004JB003399

Aubry, J., Passelègue, F. X., Deldicque, D., Girault, F., Marty, S., Lahfid, A., Bhat, H. S., Escartin, J., & Schubnel, A. (2018). Frictional Heating Processes and Energy Budget During Laboratory Earthquakes. *Geophysical Research Letters*, *45*(22), 12,274-12,282. https://doi.org/10.1029/2018GL079263

Bedford, J. D., Faulkner, D. R., & Lapusta, N. (2022). Fault rock heterogeneity can produce fault weakness and reduce fault stability. *Nature Communications*, *13*(1), 1–7. https://doi.org/10.1038/s41467-022-27998-2

Beeler, N. M., Tullis, T. E., Blanpied, M. L., & Weeks, J. D. (1996). Frictional behavior of large displacement experimental faults. *Journal of Geophysical Research B: Solid Earth*, *101*(4), 8697–8715. https://doi.org/10.1029/96jb00411

Biegel, R. L., Sammis, C. G., & Dieterich, J. H. (1989). The frictional properties of a simulated gouge having a fractal particle distribution. *Journal of Structural Geology*, *11*(7), 827–846. https://doi.org/10.1016/0191-8141(89)90101-6

Bürgmann, R. (2018). The geophysics, geology and mechanics of slow fault slip. *Earth and Planetary Science Letters*, *495*, 112–134. https://doi.org/10.1016/j.epsl.2018.04.062

Byerlee, J. D. (1978). Friction of rocks. *Pure and Applied Geophysics PAGEOPH*, *116*(4–5), 615–626. https://doi.org/10.1007/BF00876528

Byerlee, J. D., Mjachkin, V., Summers, R., & Voevoda, O. (1978). Structures developed sliding and stick-slip in fault gouge during stable. *Tectonophysics*, *44*, 161–171.

Caniven, Y., Morgan, J. K., & Blank, D. G. (2021). The Role of Along-Fault Dilatancy in Fault Slip Behavior. *Journal of Geophysical Research : Solid Earth*, 1–21. https://doi.org/10.1029/2021JB022310

Casas, N. (2022). *Insights on the behavior of fault gouges during seismic sliding: a numerical investigation from granular rheology to friction laws*. INSA Lyon.

Casas, N., Mollon, G., & Daouadji, A. (2021). Shear bands in dense fault gouge. *EPJ Web of Conferences - Powders and Grains*, *249*, 1–4. https://doi.org/10.1051/epjconf/202124911006

Casas, N., Mollon, G., & Daouadji, A. (2022). DEM Analyses of Cemented Granular Fault Gouges at the Onset of Seismic Sliding: Peak Strength, Development of Shear Zones and Kinematics. *Pure and Applied Geophysics*. https://doi.org/10.1007/s00024-021-02934-5

Cho, N., Martin, C. D., & Sego, D. C. (2008). Development of a shear zone in brittle rock subjected to direct shear. *International Journal of Rock Mechanics and Mining Sciences*, *45*(8), 1335–1346. https://doi.org/10.1016/j.ijrmms.2008.01.019

Collettini, C., Tesei, T., Scuderi, M. M., Carpenter, B. M., & Viti, C. (2019). Beyond Byerlee friction, weak faults and implications for slip behavior. *Earth and Planetary Science Letters*, *519*, 245–263. https://doi.org/10.1016/j.epsl.2019.05.011

Cundall, P. A. ., & Strack, O. D. L. (1979). A discrete numerical model for granular assemblies. *Géotechnique*, *29*(1), 47–65. https://doi.org/10.1680/geot.1979.29.1.47

Da Cruz, F., Emam, S., Prochnow, M., Roux, J. N., & Chevoir, F. (2005). Rheophysics of dense granular materials: Discrete simulation of plane shear flows. *Physical Review E*, *72*(2), 1–17. https://doi.org/10.1103/PhysRevE.72.021309

Daouadji, A., & Hicher, P. (2010). An enhanced constitutive model for crushable granular materials. *International Journal for Numerical and Analytical Methods in Geomechanics*, *34*, 555–580. https://doi.org/10.1002/nag

Davis, G. H., Bump, A. P., García, P. E., & Ahlgren, S. G. (2000). Conjugate Riedel deformation band shear zones. *Journal of Structural Geology*, *22*(2), 169–190. https://doi.org/10.1016/S0191-8141(99)00140-6

Di Toro, G., Pennacchioni, G., & Nielsen, S. (2009). Pseudotachylytes and earthquake source mechanics. In *International Geophysics* (Vol. 94, Issue C). https://doi.org/10.1016/S0074-6142(08)00005-3

Dieterich, J. H. (1972). Time-dependent friction in rocks. *Journal of Geophysical Research*, *77*(20), 3690–3697. https://doi.org/10.1029/jb077i020p03690

Dieterich, J. H. (1979). Modeling of Rock Friction Experimental Results and Constitutive Equations. *Journal of Geophysical Research*, *84*(9), 2161–2168.

Dorostkar, O., Guyer, R. A., Johnson, P. A., Marone, C., & Carmeliet, J. (2017a). On the micromechanics of slip events in sheared, fluid-saturated fault gouge. *Geophysical Research Letters*, *44*(12), 6101–6108. https://doi.org/10.1002/2017GL073768

Dorostkar, O., Guyer, R. A., Johnson, P. A., Marone, C., & Carmeliet, J. (2017b). On the role of fluids in stick-slip dynamics of saturated granular fault gouge using a coupled computational fluid dynamics-discrete

element approach. *Journal of Geophysical Research: Solid Earth*, *122*(5), 3689–3700. https://doi.org/10.1002/2017JB014099

Ferdowsi, B., Griffa, M., Guyer, R. A., Johnson, P. A., Marone, C., & Carmeliet, J. (2014). Three-dimensional discrete element modeling of triggered slip in sheared granular media. *Physical Review E*, *89*(4), 1–12. https://doi.org/10.1103/PhysRevE.89.042204

Ferdowsi, B., & Rubin, A. M. (2020). *A Granular Physics-Based View of Fault Friction Experiments*. *May*, 1–32. https://doi.org/10.1029/2019JB019016

Fondriest, M., Mecklenburgh, J., Passelegue, F. X., Artioli, G., Nestola, F., Spagnuolo, E., Rempe, M., & Di Toro, G. (2020). Pseudotachylyte Alteration and the Rapid Fade of Earthquake Scars From the Geological Record. *Geophysical Research Letters*, *47*(22), 1–9. https://doi.org/10.1029/2020GL090020

Gao, K., Euser, B. J., Rougier, E., Guyer, R. A., Lei, Z., Knight, E. E., Carmeliet, J., & Johnson, P. A. (2018). Modeling of Stick-Slip Behavior in Sheared Granular Fault Gouge Using the Combined Finite-Discrete Element Method. *Journal of Geophysical Research: Solid Earth*, *123*(7), 5774–5792. https://doi.org/10.1029/2018JB015668

Gu, Y., & Wong, T. F. (1994). Development of shear localization in simulated quartz gouge: Effect of cumulative slip and gouge particle size. *Pure and Applied Geophysics PAGEOPH*, *143*(1–3), 387–423. https://doi.org/10.1007/BF00874336

Guo, Y., & Morgan, J. K. (2004). Influence of normal stress and grain shape on granular friction: Results of discrete element simulations. *Journal of Geophysical Research: Solid Earth*, *109*(B12). https://doi.org/10.1029/2004JB003044

Hadizadeh, J., Tullis, T. E., White, J. C., & Konkachbaev, A. I. (2015). Shear localization, velocity weakening behavior, and development of cataclastic foliation in experimental granite gouge. *Journal of Structural Geology*, *71*, 86–99. https://doi.org/10.1016/j.jsg.2014.10.013

Haines, S. H., Kaproth, B., Marone, C., Saffer, D., & Van der Pluijm, B. (2013). Shear zones in clay-rich fault gouge: A laboratory study of fabric development and evolution. *Journal of Structural Geology*, *51*, 206–225. https://doi.org/10.1016/j.jsg.2013.01.002

Hirata, M., Muto, J., & Nagahama, H. (2017). Shear zone development and frictional instabilities. *International Journal of GEOMATE*, *12*(34), 32–37. https://doi.org/10.21660/2017.34.2660

Im, K., Marone, C., & Elsworth, D. (2019). The transition from steady frictional sliding to inertia-dominated instability with rate and state friction. *Journal of the Mechanics and Physics of Solids*, *122*, 116–125. https://doi.org/10.1016/j.jmps.2018.08.026

Im, K., Saffer, D., Marone, C., & Avouac, J. P. (2020). Slip-rate-dependent friction as a universal mechanism for slow slip events. *Nature Geoscience*, *13*(10), 705–710. https://doi.org/10.1038/s41561-020-0627-9

Jiao, L., Klinger, Y., & Scholtès, L. (2021). Fault Segmentation Pattern Controlled by Thickness of Brittle Crust. *Geophysical Research Letters*, *48*(19), 1–7. https://doi.org/10.1029/2021GL093390

Kaminskaite, I., Fisher, Q. J., & Michie, E. A. H. (2019). Microstructure and petrophysical properties of deformation bands in high porosity carbonates. *Journal of Structural Geology*, *119*(December 2018), 61–80. https://doi.org/10.1016/j.jsg.2018.12.001

Kanamori, H., & Heaton, T. H. (2000). Microscopic and Macroscopic Physics of Earthquakes. In J. B. Rundle, D. L. Turcotte, & W. Klein (Eds.), *Geocomplexity and the Physics of Earthquakes* (pp. 147–163). https://doi.org/10.1029/GM120p0147

Katz, Y., & Weinberger, R. (2005). Strain localization in sandstone during embryonic stages of shear-zone evolution. *Terra Nova*, *17*(4), 311–316. https://doi.org/10.1111/j.1365-3121.2005.00615.x

Katz, Y., Weinberger, R., & Aydin, A. (2004). Geometry and kinematic evolution of Riedel shear structures, Capitol Reef National Park, Utah. *Journal of Structural Geology*, *26*(3), 491–501. https://doi.org/10.1016/j.jsg.2003.08.003

Ke, C. Y., McLaskey, G. C., & Kammer, D. S. (2022). Earthquake breakdown energy scaling despite constant fracture energy. *Nature Communications*, *13*(1), 1–8. https://doi.org/10.1038/s41467-022-28647-4

Lee, H. K., & Kim, H. S. (2005). Comparison of structural features of the fault zone developed at different protoliths: Crystalline rocks and mudrocks. *Journal of Structural Geology*, *27*(11), 2099–2112. https://doi.org/10.1016/j.jsg.2005.06.012

Leeman, J., Saffer, D., Scuderi, M., & Marone, C. (2016). Laboratory observations of slow earthquakes and the spectrum of tectonic fault slip modes. *Nature Communications*, *7*, 1–6. https://doi.org/10.1038/ncomms11104

Leeman, J., Scuderi, M. M., Marone, C., & Saffer, D. (2015). Stiffness evolution of granular layers and the origin of repetitive, slow, stick-slip frictional sliding. *Granular Matter*, *17*(4), 447–457. https://doi.org/10.1007/s10035-015-0565-1

Lefevre, M., Souloumiac, P., Cubas, N., & Klinger, Y. (2020). Experimental evidence for crustal control over seismic fault segmentation. *Geology*, *48*(8), 844–848. https://doi.org/10.1130/G47115.1

Lynch, J. C., & Richards, M. a. (2001). Finite element models of stress orientations in well-developed strike-slip

fault zones: Implications for the distribution of lower crustal strain. *Journal of Geophysical Research*, *106*(B11), 26,707-26729. https://doi.org/0148-0227/01/2001JB000289509

Lyu, Z., Rivière, J., Yang, Q., & Marone, C. (2019). On the mechanics of granular shear: The effect of normal stress and layer thickness on stick-slip properties. *Tectonophysics*, *763*(April), 86–99. https://doi.org/10.1016/j.tecto.2019.04.010

Mair, K., Frye, K. M., & Marone, C. (2002). Influence of grain characteristics on the friction of granular shear zones. *Journal of Geophysical Research: Solid Earth*, *107*(B10), ECV 4-1-ECV 4-9. https://doi.org/10.1029/2001JB000516

Marone, C. (1998). Laboratory-derived friction laws and their application to seismic faulting. *Annual Review of Earth Planetary Sciences*, *26*, 643–696. https://doi.org/10.1146/annurev.earth.26.1.643

Marone, C., & Scholz, C. H. (1988). The depth of seismic faulting and the upper transition from stable to unstable slip regimes. *Geopgysical Reschearch Letters*, *15*(8), 621–624. https://doi.org/10.1029/GL015i006p00621

Marone, C., & Scholz, C. H. (1989). Particle-size distribution and microstructures within simulated fault gouge. *Journal of Structural Geology*, *11*(7), 799–814. https://doi.org/10.1016/0191-8141(89)90099-0

McLaskey, G. C. (2019). Earthquake Initiation From Laboratory Observations and Implications for Foreshocks. *Journal of Geophysical Research: Solid Earth*, *124*(12), 12882–12904. https://doi.org/10.1029/2019JB018363

Mollon, G. (2016). A multibody meshfree strategy for the simulation of highly deformable granular materials. *International Journal for Numerical Methods in Engineering*, *108*(12), 1477–1497. https://doi.org/10.1002/nme.5258

Mollon, G. (2018). A unified numerical framework for rigid and compliant granular materials. *Computational Particle Mechanics*, *5*, 517–527. https://doi.org/10.1007/s40571-018-0187-6

Mollon, G., Aubry, J., & Schubnel, A. (2021). Simulating Melting in 2D Seismic Fault Gouge. *Journal of Geophysical Research: Solid Earth*, *126*(6), 1–19. https://doi.org/10.1029/2020JB021485

Mollon, G., Quacquarelli, A., Andò, E., & Viggiani, G. (2020). Can friction replace roughness in the numerical simulation of granular materials? *Granular Matter*, *22*(42). https://doi.org/10.1007/s10035-020-1004-5

Mollon, G., & Zhao, J. (2012). Fourier-Voronoi-based generation of realistic samples for discrete modelling of granular materials. *Granular Matter*, *5*, 621–638. https://doi.org/10.1007/s10035-012-0356-x

Moore, D. E., & Byerlee, J. D. (1992). Relationships between sliding behavior and internal geometry of laboratory fault zones and some creeping and locked strike-slip faults of California. *Tectonophysics*, *211*(1–4), 305–316. https://doi.org/10.1016/0040-1951(92)90067-G

Moore, D. E., Summers, R., & Byerlee, J. D. (1989). Sliding behavior and deformation textures of heated illite gouge. *Journal of Structural Geology*, *11*(3), 329–342. https://doi.org/10.1016/0191-8141(89)90072-2

Morgan, J. K. (1999). Numerical simulations of granular shear zones using the distinct element method: 2. Effects of particle size distribution and interparticle friction on mechanical behavior. *Journal of Geophysical Research: Solid Earth*, *104*(B2), 2721–2732. https://doi.org/10.1029/1998jb900055

Morgan, J. K., & Boettcher, M. S. (1999). Numerical simulations of granular shear zones using the distinct element method: 1. Shear zone kinematics and the micromechanics of localization. *Journal of Geophysical Research: Solid Earth*, *104*(B2), 2703–2719. https://doi.org/10.1029/1998jb900056

Nouguier-lehon, C., Cambou, B., & Vincens, E. (2003). Influence of particle shape and angularity on the behaviour of granular materials : a numerical analysis. *International Journal for Numerical and Analytical Methods in Geomechanics*, *27*(14), 1207–1226. https://doi.org/10.1002/nag.314

Ohnaka, M. (2013). *The physics of Rock Failure and Earthquakes*. Cambridge University Press. https://doi.org/10.1017/CBO9781139342865

Orellana, L. F., Scuderi, M. M., Collettini, C., & Violay, M. (2018). Do scaly clays control seismicity on faulted shale rocks? *Earth and Planetary Science Letters*, *488*, 59–67. https://doi.org/10.1016/j.epsl.2018.01.027

Paglialunga, F., Passelègue, F. X., Brantut, N., Barras, F., Lebihain, M., & Violay, M. (2021). On the scale dependence in the dynamics of frictional rupture : constant fracture energy versus size-dependent breakdown work. *Preprint in Earth and Planetary Science Letters*, *584*, 1–33. https://doi.org/10.1016/j.epsl.2022.117442

Passelègue, F. X., Aubry, J., Nicolas, A., Fondriest, M., Deldicque, D., Schubnel, A., & Di Toro, G. (2019). From fault creep to slow and fast earthquakes in carbonates. *Geology*, *47*(8), 744–748. https://doi.org/10.1130/G45868.1

Potyondy, D. O., & Cundall, P. A. (2004). A bonded-particle model for rock. *International Journal of Rock Mechanics and Mining Sciences*, *41*(8), 1329–1364. https://doi.org/10.1016/j.ijrmms.2004.09.011

Rabinowicz, E. (1951). The nature of the static and kinetic coefficients of friction. *Journal of Applied Physics*, *22*(11), 1373–1379. https://doi.org/10.1063/1.1699869

Reches, Z., & Lockner, D. A. (2010). Fault weakening and earthquake instability by powder lubrication. *Nature*, *467*(7314), 452–455. https://doi.org/10.1038/nature09348

Rice, J. R., & Cocco, M. (2002). Seismic Fault Rheology and Earthquake Dynamics. *Journal of Geophysical*

Research, *107*, 1000–1029.
Riedel, W. (1929). Zur Mechanik geologischer Brucherscheinungen ein Beitrag zum Problem der Fiederspatten. *Zentbl. Miner. Geol. Palaont. Abt.*, 354–368.
Riedmüller, B. G., Brosch, F. J., Klima, K., & Medley, E. W. (2001). Engineering Geological Characterization of Brittle Faults and classification of fault rocks. *Engineering Geology*, *19*(April), 13–19.
Rodrigues, R. de S., Alves da Silva, F. C., & Córdoba, V. C. (2021). Evolution of deformation bands, insights from structural diagenesis. *Journal of Structural Geology*, *143*(December 2020). https://doi.org/10.1016/j.jsg.2020.104257
Sammis, C. G., King, G., & Biegel, R. (1987). The kinematics of gouge deformation. *Pure and Applied Geophysics*, *125*, 777–812. https://doi.org/10.1007/BF00878033
Scholz, C. H. (1987). Wear and gouge formation in brittle faulting. *Geology*, *15*(6), 493–495. https://doi.org/10.1130/0091-7613(1987)15<493:WAGFIB>2.0.CO;2
Scholz, C. H. (2002). *The Mechanics of Earthquakes and Faulting*, *second edition* (Cambridge). https://doi.org/10.2113/gseegeosci.13.1.81
Scholz, C. H., Molnar, P., & Johnson, T. (1972). Detailed studies of frictional sliding of granite and implications for the earthquake mechanism. *Journal of Geophysical Research*, *77*(32), 6392–6406. https://doi.org/10.1029/jb077i032p06392
Scuderi, M. M., Tinti, E., Cocco, M., & Collettini, C. (2020). The Role of Shear Fabric in Controlling Breakdown Processes During Laboratory Slow-Slip Events. *Journal of Geophysical Research: Solid Earth*, *125*(11). https://doi.org/10.1029/2020JB020405
Spagnuolo, E., Nielsen, S., Violay, M., & Di Toro, G. (2016). An empirically based steady state friction law and implications for fault stability. *Geophysical Research Letters*, *43*(7), 3263–3271. https://doi.org/10.1002/2016GL067881
Tchalenko, J. S. (1970). Similarities between shear zones of different magnitudes. *Geological Society Of America Bulletin*, *81*(6), 1625–1640. https://doi.org/10.1130/0016-7606(1970)81[1625:SBSZOD]2.0.CO;2
Walderhaug, O. (1994). Precipitation rates for quartz cement in sandstones determined by fluid-inclusion microthermometry and temperature-history modeling. *Journal of Sedimentary Research A: Sedimentary Petrology & Processes*, *64 A*(2), 324–333. https://doi.org/10.2110/jsr.64.324
Woodcock, N. H., & Mort, K. (2008). Classification of fault breccias and related fault rocks. *Geological Magazine*, *145*(3), 435–440. https://doi.org/10.1017/S0016756808004883
Zhao, Z. (2013). Gouge particle evolution in a rock fracture undergoing shear: A microscopic DEM study. *Rock Mechanics and Rock Engineering*, *46*(6), 1461–1479. https://doi.org/10.1007/s00603-013-0373-z
Zhao, Z., Jing, L., & Neretnieks, I. (2012). Particle mechanics model for the effects of shear on solute retardation coefficient in rock fractures. *International Journal of Rock Mechanics and Mining Sciences*, *52*, 92–102. https://doi.org/10.1016/j.ijrmms.2012.03.001